GFZ

Helmholtz-Zentrum

POTSDAM

Originally published as:

Localised thickening and grounding of an Antarctic ice shelf from tidal triggering and sizing of cryoseismicity

Myrto Pirli[a], Sebastian Hainzl[b], Johannes Schweitzer[c,d], Andreas Köhler[e] and Torsten Dahm[b,f]

[a] Tårnbyveien 370, 2013 Skjetten, Norway, e-mail: myrto.pirli@gmail.com

[b] GFZ German Research Centre for Geosciences, Telegrafenberg, 14473 Potsdam, Germany, e-mail: hainzl@gfz-potsdam.de, torsten.dahm@gfz-potsdam.de

[c] NORSAR, Gunnar Randers vei 15, 2007 Kjeller, Norway, e-mail: johannes.schweitzer@norsar.no

[d] Centre for Earth Evolution and Dynamics (CEED), University of Oslo, P.O. Box 1028 Blindern, 0315 Oslo, Norway

[e] Department of Geosciences, University of Oslo, P.O. Box 1047 Blindern, 0316 Oslo, Norway, e-mail: andreas.kohler@geo.uio.no

[f] Institute of Earth and Environmental Sciences, University of Potsdam, 14476 Potsdam, Germany.

Corresponding author: Myrto Pirli, e-mail: myrto.pirli@gmail.com

Abstract

We observe remarkably periodic patterns of seismicity rates and magnitudes at the Fimbul Ice Shelf, East Antarctica, correlating with the cycles of the ocean tide. Our analysis covers 19 years of continuous seismic recordings from Antarctic broadband stations. Seismicity commences abruptly during austral summer 2011 at a location near the ocean front in a shallow water region. Dozens of highly repetitive events occur in semi-diurnal cycles, with magnitudes and rates fluctuating steadily with the tide. In contrast to the common

27 unpredictability of earthquake magnitudes, the event magnitudes show deterministic trends

28 within single cycles and strong correlations with spring tides and tide height. The events

29 occur quasi-periodically and the highly constrained event sources migrate landwards during

30 rising tide. We show that a simple, mechanical model can explain most of the observations.

31 Our model assumes stick-slip motion on a patch of grounded ice shelf, which is forced by

32 the variations of the ocean-tide height and ice flow. The well fitted observations give new

33 insights into the general process of frictional triggering of earthquakes, while providing

34 independent evidence of variations in ice shelf thickness and grounding.

35

36 **Keywords**

37 tidally modulated cryogenic seismicity; stick-slip motion; event recurrence predictability; ice-

38 shelf thickness; ice-shelf grounding; East Antarctica

39 [1]

40

41 **1. Introduction**

42 In recent years, repetitive tide-modulated seismicity has been discovered at glaciers and ice

43 shelves in Antarctica (e.g., Barruol et al., 2013; Hammer et al., 2015; Lombardi et al., 2016;

44 Winberry et al., 2014; Zoet et al., 2012) and Greenland (Podolskiy et al., 2016). Typically

45 observed near the grounding zone, it shows a wide variety of temporal patterns and

46 correlations with the components of the ocean tide, which can be used as diagnostic tools to

47 assess the driving mechanisms of this type of cryogenic seismicity and potential links to

48 glacial dynamics. Main interpretations involve stick-slip motion at the ice/bedrock interface

---

[1]Abbreviations
CC   Cross-correlation
CFS   Coulomb Failure Stress
DML   Dronning Maud Land
FIS   Fimbul Ice Shelf
HMM   Hidden Markov Model
SNR   Signal-to-noise ratio
STA   Short-term average

49 (e.g., Barruol et al., 2013; Lombardi et al., 2016; Winberry et al., 2014; Zoet et al., 2012) and

50 brittle deformation of the ice shelf due to tidal flexure (Barruol et al., 2013; Hammer et al.,

51 2015; Lombardi et al., 2016), all recognizing the importance of stress and strain rate

52 variations to the triggering of cryoseismic activity (e.g., Bindschadler et al., 2003; Hammer et

53 al., 2015; Podolskiy et al., 2016; Winberry et al., 2014). However, relevant studies often

54 have short observation intervals, due to the need for dedicated field deployments (e.g.,

55 Lombardi et al., 2016; Podolskiy et al., 2016), the longest ranging ones reporting one or

56 more non-consecutive intervals of about a year (Barruol et al., 2013; Hammer et al., 2015;

57 Winberry et al., 2014).

58

59 The study focuses on the Fimbul Ice Shelf (FIS), in Dronning Maud Land (DML), East

60 Antarctica. The main contributor to the ice shelf is the outlet of the Jutulstraumen glacier,

61 whose ice tongue, the Trolltunga, partly extends past the continental shelf break into the

62 Weddell Sea (Fig. 1a). The differential flow between the fast-flowing central part of the outlet

63 glacier and the much slower lateral parts of the shelf (e.g., Rignot et al., 2011) creates zones

64 of shear deformation, characterised by abundant crevasses and rifts (Humbert and

65 Steinhage, 2011). Although the central basin of the FIS cavity has a deep seabed (e.g.,

66 Nøst, 2004), near the calving front, the ice shelf becomes locally grounded on shallow

67 bathymetric features that either divert ice flow (ice rises) or allow it to continue over them

68 (ice rumples) (Matsuoka et al., 2015; van Oostveen et al., 2017).

69

70 We present seismic records of an almost two decade long continuous monitoring of a

71 specific source region at the FIS, showing emergent activity and trends over several years

72 with strikingly similar and regular seismic events near the ocean front, in an area of outcrops

73 of bedrock. A key question is whether the distinct seismicity pattern can be explained with

74 established, physics-based models of earthquake triggering, and whether environmental

75 drivers can be identified and quantified. We employ a simple mechanical model based on

76   tidally modulated shear and normal stress and demonstrate that this activity is likely related

77   to stick-slip motion of the thickened ice shelf, which is newly grounded on a shallow

78   bathymetric feature.

79

80   **2. Data and methods**

81   **2.1 Data**

82   We use waveform data from the permanent, international seismic network in DML (Fig. 1a).

83   Continuous data are used from the broadband, three-component stations SNAA and

84   TROLL, situated at the South African research station SANAE IV and the Norwegian station

85   Troll, respectively. Employed SNAA records span the time-period March 1997 to end 2015,

86   and TROLL data February 2012 to end 2015. In addition, we use selected records from the

87   Watzmann seismic array, deployed around station VNA2, both belonging to the seismic

88   network of the German research station Neumayer III.

89

90   Ocean tide heights for the study region, sampled at each full minute, are estimated from the

91   high-resolution regional inverse tide model CATS2008a_opt (Padman et al., 2002, 2008) for

92   the ocean around Antarctica, including the areas under the floating ice shelves. GPS

93   measurements (Kohler and Langley, 2016) obtained in November 2010 at a location near

94   the study region (~ 30 km to the SSE) are used to assess the accuracy of the predicted tidal

95   phase.

96

97   **2.2 Compilation of cryoseismic event catalogue**

98   2.2.1 Detection by waveform cross-correlation

99   The observed cryoseismic events have so similar waveforms that they can be identified by

100   visual inspection (Fig. 2). Therefore, we compile our event catalogue using the array-based

101   waveform cross-correlation (CC) detector of Gibbons and Ringdal (2006). Small magnitude

102   events are detected through the enhancement of signal-to-noise ratio (SNR), by stacking the

103   correlation traces for all individual channels of a seismic array or a single, three-component

104   station. Master template events (Table S1 in Supplementary Material), selected to have

105   sufficiently high SNR and to sample adequately intervals of high activity, as well as to cover

106   the entire duration of the study, run through the continuous waveform records of TROLL and

107   SNAA in search of similar events, based on a user defined SNR threshold. The master

108   templates employ the entire body-wave wavetrain, with a length of 50 s for TROLL and 45 s

109   for SNAA, bandpass filtered in the frequency range of maximum SNR (2 – 6 Hz). Detection

110   thresholds (SNR, CC-coefficient) are defined through visual inspection of a large sample of

111   results, accepting detections for SNR larger than 10, and only considering CC-coefficient

112   values higher than 0.40.

113

114   2.2.2 Detection with a Hidden Markov Model classifier

115   CC-detector results are compared to those of a Hidden Markov Model (HMM) classifier

116   (Hammer et al., 2013; references therein) (Fig. S1 in Supplementary Material), a

117   probabilistic approach able to statistically capture the intrinsic variability of the characteristics

118   of a class of seismic signals. The observed data are modelled by a sequence of hidden,

119   unobserved states, each assumed to emit observations according to a particular emission

120   probability (see Supplementary Material for details). These observations are obtained by

121   parametrizing the seismic signal by a time series of feature vectors (here, spectral power in

122   different frequency bands). An HMM is then trained by estimating the probability distribution

123   of the features at each state and the transition probabilities (see Supplementary Material)

124   between the states using a pre-selected training data set with known class labels (i.e., event

125   type). The classifier must also include a class for the seismic background noise. In the

126   current implementation, event states and their probabilities are estimated from seismic

127   background noise data modelled by Gaussian mixtures, and the event HMM is initially

128   trained using a single seismic signal (Hammer et al., 2013; references therein).

129

130   The trained classifier is applied on all available continuous TROLL data in 2013. An event is

131   reported if the probability of the event HMM is larger than that of the noise HMM in a given

132   data window. Post-processing includes merging detections belonging to the same event in

133   consecutive classification windows and removing all events with too low absolute

134   probabilities and too small probability differences compared to the noise HMM. In addition,

135   the SNR is used to reject false positives. An extended description of the method and

136   specifics on its implementation herein can be found in the Supplementary Material.

137

138   **2.3 Cryoseismic event location**

139   The source of the cryoseismic events is located using the seismic event location routine

140   HYPOSAT (Schweitzer, 2001, 2018). To obtain an estimate as accurate as possible and

141   considering the small magnitude of the events, we read seismic phase onsets on the

142   summation trace (beam) for the Watzmann array (e.g., Schweitzer et al., 2012) and the

143   summed traces of events with CC-coefficients larger than 0.90 (multiplets) for stations

144   TROLL and SNAA. In addition to absolute onset times, travel-time differences between the

145   employed seismic phase onsets (Sn - Pn) are used. The apparent velocity and backazimuth

146   of the seismic phases are determined through array-data processing (e.g., Schweitzer et al.,

147   2012) for the array and three-component analysis (Schweitzer, 2013) for the single stations.

148   The seismic velocity model (Fig. S2 in Supplementary Material) that provides the best fit to

149   the observations describes the crust and upper mantle in the region based on information

150   from local (Nøst, 2004) and regional studies (Bayer et al., 2009; Torsvik, 2015). Focal depth

151   is kept fixed at the surface (ice – bedrock interface), since the recording network does not

152   provide adequate resolution to invert for it (e.g., Havskov et al., 2012).

153

154   The small magnitude of the events (largest ~ 1.2, see section 2.4) and the distance to the

155   seismic stations do not facilitate the location of the volume of detected events. Instead, we

156   determine the size of the activated area based on fluctuations in the time difference of

157 seismic onsets at TROLL and SNAA that are translatable into corresponding differences in

158 source location. We estimate the corresponding difference in travel-time, add this change

159 (0.060 s for TROLL and 0.099 s for SNAA) to the S-P difference of our absolute location

160 estimate, and obtain a new solution that expresses the spatial extent of the activated area.

161 Larger time differences between TROLL and SNAA than those of the event used for the

162 absolute location imply that the corresponding sources are farther away from the stations

163 than the reference location.

164

165 **2.4 Event magnitude estimates**

166 For our dataset, magnitude is defined as the logarithmic maximum amplitude, A_{max}, between

167 the vertical, radial and transverse component for each of the stations TROLL and SNAA:

168 $M = \log_{10} A_{max}$ (1)

169 For this purpose, we construct short-term averaged (STA) traces of waveforms filtered

170 between 2 and 4 Hz, using a window length of 1.4 s, and measure the maximum amplitude

171 within a 20 s long window that contains the S-wave. We correct for the instrument response

172 of each station, to obtain amplitudes in nm/s.

173 The result is a self-consistent magnitude scale for this specific population of seismic events,

174 where it is size relations between events that are important and not absolute values.

175

176 **3. Observations**

177 **3.1 Spatiotemporal characteristics of cryoseismicity**

178 The recorded activity is manifested as highly similar, small magnitude events that exhibit

179 very alike temporal patterns at stations TROLL and SNAA. One of the best recorded

180 cryoseismic events occurred on 9 September 2013 04:40:20.3 UTC and had a station

181 magnitude at TROLL of $M = 1.16$. It is located at 70.031°S ± 0.025°, 0.452°E ± 0.035° on the

182 outlet of the Jutulstraumen glacier, near the front of the FIS to the ocean, at distances of 220

183 – 230 km from the nearest seismic stations SNAA and TROLL, and 310 km from VNA2 (Fig.

184 1a,b). Our relative location scheme (section 2.3) shows that the events are taking place at

185 an area with a largest length of about 470 m, trending almost N-S, with the absolute location

186 estimate near its southern border (inlet of Fig. 1b).

187

188 The complete catalogue of events obtained using the CC-detector (section 2.2) contains

189 altogether about 10000 cryoseismic events between March 1997 and end 2015, covering

190 almost two decades (Fig. 1c and Fig. S1 in Supplementary Material). The earliest findings

191 are low-level activity in 2003 and a few isolated events between 2005 and 2009. From late

192 2011 on, the observed level of cryoseismicity increases, varying between intervals without

193 any events to high intensity phases with tens of events per day. In general, activity

194 intensifies during the austral winter-spring months and decreases or pauses from summer

195 through autumn, with the maximum levels fluctuating from year to year. This seasonal

196 pattern has similarities to that observed along the DML coast West of Trolltunga, near the

197 Neumayer III station in 2004 (Hammer et al., 2015), although a systematic comparison is

198 inhibited by a lack of data during the entire austral spring season in that study.

199

200 We focus on the most intense seismic activity between August and October 2013 that is

201 characterised by the highest waveform similarity levels (CC-coefficients in Fig. S1 in

202 Supplementary Material). We use TROLL data to take advantage of the higher sampling rate

203 and the better SNR conditions compared to SNAA (Schweitzer et al., 2014). Confidence in

204 the CC-detector results is strengthened by the very similar patterns retrieved from SNAA

205 and TROLL (Fig. S1 in Supplementary Material). The distributions at the two stations differ

206 slightly in the number of detected events, mainly due to diverse noise conditions that affect

207 the performance of the master event templates. However, the general activity patterns are

208 the same at the two stations. The robustness of the results is evaluated by comparing the

209 CC-detector results against the findings of the HMM classifier (section 2.2), which

210 corroborates the observed temporal pattern (Fig. S1 in Supplementary Material). Although

the HMM method provides a slightly less complete catalogue for 2013 than the CC-detector,

it results in a similar distribution. The HMM classifier is trained with spectral features that

should allow for some degree of waveform variability within the event class. The similarity in

results therefore suggests that no significant number of seismic signals with slightly different

waveforms compared to the master events is missed by the CC-detector.

3.2 Tidal modulation of cryoseismicity

We observe strong correlations between the timing and magnitude of the events (blue

symbols in Figs. 3 and 4) with the amplitude of the ocean tide. Within the 14-day tidal cycle,

a clear correlation is found between event rates and tidal amplitude, with almost double as

many events around spring tides than around neap tides (Fig. 3a,b). The tides also modulate

the event magnitude distribution, with highly deterministic patterns being observed within

each semi-diurnal tidal cycle. A clear magnitude trend occurs that differs depending on the

proximity of the cycle to the neap or the spring tide (Fig. 3c-e). For quantification, we

calculate for each cluster (defined by sequences of a minimum of 5 events with inter-event

times less than 6 hours) the average magnitude difference, $\langle \Delta M \rangle$ (blue points in Fig. 3c). The

result indicates negative trends ($\langle \Delta M \rangle < 0$) during spring tides and increasing magnitudes

during neap tides ($\langle \Delta M \rangle > 0$). Exemplary clusters are shown in Fig. 3d,e, illustrating the

increasing magnitudes during neap tides (Fig. 3d) and an almost linear decrease during

spring tides (Fig. 3e). Similar trends can be also seen for the other clusters in the analysed

time period (see time series in Fig. S3, Supplementary Material).

In all cases, the events occur quasi-periodically indicating that each event leads to a partial

unloading of the system. All events occur with a waiting time of at least 3 min after the

preceding event and most of them with an inter-event time of 5-10 min (Fig. 4a), a feature

that is present in the results of both detection methods and thereby not an artifact. The

observed peaked inter-event time distribution (histogram in Fig. 4a) is in contrast to random

238 occurrences, which would be expressed by an exponential interevent-time distribution. By

239 assigning a 360° phase cycle to two successive tidal maxima, we find that icequakes are

240 predominantly triggered during rising tides and stop after the maximum height of the tide has

241 been reached within each 12-hour cycle (histogram in Fig. 4b). The maximum frequency is

242 observed just before the tide reaches its peak, followed by an almost complete lack of

243 occurrences at falling tides, although we cannot exclude the occurrence of events at low

244 tides with magnitudes too small to record at the distance of observation (> 200 km). This

245 temporal pattern is quite similar to that of tidally modulated seismicity at other places in DML

246 (Hammer et al., 2015; Lombardi et al., 2016), although not all individual features are

247 common; however, Hammer et al. (2015) do not separate between different source regions,

248 while the results of Lombardi et al. (2016) are based only on one month of data.

249

250 Besides the deterministic magnitude and timing patterns, we observe systematic changes in

251 the difference between CC-detection times at TROLL and SNAA (ΔCC), which imply a shift

252 in source locations (see ΔCC-time series in Fig. S4, Supplementary Material). The ΔCC-

253 value is found to decrease within clusters at the end of the 12-hour cycles; in particular, the

254 difference of the ΔCC value between event pairs is shown to be linearly correlated to the

255 occurrence time difference of the event pair (Fig. 4c). This result indicates a systematic

256 migration of the activity within the 12-hour cycles, in a landward direction opposite of the ice

257 flow (Fig. 1b and inlet). This is consistent with the observations of Brunt et al. (2011) and

258 models of tidal migration of ice-shelf grounding lines (e.g., Sayag and Worster, 2013; Tsai

259 and Gudmundsson, 2015) that attribute slip during high tides to increased lubrication in the

260 system. Finally, the event magnitudes are found to correlate with the tidal amplitudes.

261 Although a broad range of event magnitude values are observed for different tide heights,

262 Fig. 4d shows a positive trend for small tidal levels, while a reversed trend is found for larger

263 levels, as already seen in Fig. 3d,e.

264

4. Modelling

4.1 Model setup

The observed suite of temporal, magnitude and migration features provides strong constraints for modelling. Our model is based on an assumption that the observed cryogenic events result from basal stick-slip motion of the ice shelf on a localized grounding feature (ice shelf pinning point in e.g., Robel et al., 2017), as shown in the schematic plot of Fig. 5a. Loading occurs due to an increase in shear stress related to ice flow, as well as changes of the normal stress, both modulated by the tidal amplitude. Slip is initiated when the Coulomb Failure Stress (*CFS*) exceeds a critical level in the contact area between the base of the ice shelf and the bedrock protrusion.

The main model variable effecting the stress state, the hypocentre location, and the event magnitude, is the difference Δ between the elevation z_2 of the peak of the local grounding region (bedrock protrusion) and the elevation z_1 of the bottom of the ice shelf, when the latter is considered to be freely floating. This referencing is a valid approximation if the ice shelf is only slightly elevated at the bedrock protrusion (see Fig. 5a and Table 1 for a description of the model parameters). The Δ-value varies on short-time scale due to tidal variations $h(t)$ and on long-time scales due to ice shelf thinning or thickening. Stick-slip motion can only occur for $\Delta > 0$ and the contact area between the grounding point and the bottom of the ice shelf increases for increasing Δ-values. Considering that the density of glacial ice is approximately 90% of the water density and the ice shelf has a thickness W, the bottom of the ice shelf is located at $h(t) - 0.9W$ relative to the average sea-level. With parameter H defined as the average Δ-value in our analysed time period in 2013, the temporal variation of $\Delta(t)$ is given by $\Delta(t) = H - h(t) + 0.9\,(W - W_{2013})$, where W_{2013} is the average thickness of the ice shelf during this 80-day time interval.

291   In our simplified kinematic modelling, the Δ-value directly determines the contact area and

292   the stress state at any time, as well as the magnitude and the hypocentre location at times

293   when failure occurs:

294

295   1. Contact area: The contact area increases for increasing Δ-values. Although the

296   actual area where stick-slip occurs can be smaller, for simplicity we assume that it

297   coincides with the geometrical contact area. While actual conditions are more

298   complex, e.g., our geometry does not account for the hinge zone and

299   bending/flexuring of the ice (e.g., Vaughan, 1995; Hulbe et al., 2016), we simply

300   approximate the contact area as the cut surface of the ice shelf with an elliptical

301   topography with circular base area of maximum radius R_{max}, which leads to:

302
$$A(\Delta) = \begin{cases} 0 & for\ \Delta \leq 0 \\ \pi R_{max}^2 \left[1 - \left(1 - \frac{\Delta}{H} \right)^2 \right] & for\ 0 < \Delta < H \\ \pi R_{max}^2 & for\ \Delta \geq H \end{cases} \qquad (2)$$

303   Our assumption that A is fixed for $\Delta > H$ is not crucial because almost no events

304   occur at those times. For $0 < \Delta < H$, Δ decreases during increasing tides, leading to a

305   migration of the grounding line on the bedrock protrusion within the tidal cycles,

306   which has been observed for ice shelves before (Brunt et al. 2011). For $\Delta < 0$, the

307   bottom of the freely floating ice shelf is above the peak of the bedrock protrusion, and

308   the contact is completely lost.

309

310   2. Stress: The Coulomb-Failure stress is defined as $CFS = \tau - f\sigma_n$ with the friction

311   coefficient f, the shear stress τ, and normal stress σ_n. The shear stressing rate is

312   assumed to be proportional to the ice-flow velocity, which has been previously

313   observed to be positively correlated predominantly with the 14-day, but also the

314   semi-diurnal tidal cycles (Murray et al., 2007), a fact that is also suggested by the

315   observed 14-day rate-cycles of the analysed activity (Fig. 3a). Although reality is

316   more complex, we thus simply assume that the shear stressing rate is proportional to

317   the tidal amplitude, $\dot{\tau}(t) = \dot{\tau}_0(t) E_h(t)/\langle E_h \rangle$, where $\dot{\tau}_0$ is the average shear stressing

318   rate and E_h (shown in Fig. 3a as grey line) is the envelope of the tidal variations with

319   mean $\langle E_h \rangle$. Note that the envelope only leads to fortnightly but no diurnal variations of

320   the shear stressing rate. For an evaluation of the impact of this assumption, the

321   results for a constant shear stressing rate are shown in Fig. S5 in Supplementary

322   Material. They indicate that all features besides the 14-day rate-cycle are similarly

323   well reproduced and thus not crucially dependent on shear stressing variations.

324   The second component of the *CFS*-value, the normal stress σ_n, depends on Δ and

325   thus is also time dependent. For a first-order approximation, we use the analytic point

326   force solution for a deflection of Δ at the centre of an infinite elastic plate overlying an

327   inviscid fluid, which yields a linear relation between the point force F and Δ, $F = c_f \Delta$,

328   where the proportionality factor c_f depends on the elastic parameters, the thickness

329   W of the elastic plate, and the density contrast (Brotchie and Silvester, 1969; Jha et

330   al., 2017). Thus, the normal stress acting within the contact area $A(t)$ can be

331   approximated by $\sigma_n(t) = c_f \Delta(t)/A(t)$, and the *CFS* becomes:

332       $$CFS(t) = CFS(t_0) + \dot{\tau}_0 \int_{t_0}^{t} E_h(\tilde{t})/\langle E_h \rangle d\tilde{t} - f c_f \Delta(t)/A(\Delta(t)) \qquad (3)$$

333   To get rid of undetermined parameters, we considered the normalized stress $S =$

334       $CFS / \widetilde{CFS}$, which can be expressed by substitution using Eqs. (2) and (3) as:

335       $$S(t) = \begin{cases} 0 & for\ \Delta(t) \leq 0 \\ S(t_0) + C \int_{t_0}^{t} E_h(\tilde{t})/\langle E_h \rangle d\tilde{t} - \frac{\Delta(t)}{H}\left[1 - \left(1 - \frac{\Delta(t)}{H}\right)^2\right]^{-1} & for\ 0 < \Delta(t) < H \\ S(t_0) + C \int_{t_0}^{t} E_h(\tilde{t})/\langle E_h \rangle d\tilde{t} - \frac{\Delta(t)}{H} & for\ \Delta(t) \geq H \end{cases}$$

336   (4)

337   with $\widetilde{CFS} = f c_f H/(\pi R^2_{max})$ and $C = \dot{\tau}_0/\widetilde{CFS}$. Each icequake is assumed to lead to a

338   constant shear stress drop S_Δ at origin time t_0. For simplicity we assume

339   instantaneous healing, and the next event is triggered when the stress is reloaded,

340   i.e., if $S(t) - S(t_0) \geq S_\Delta$. An example of the temporal evolution of the stress

341   components during a 12-hour tidal cycle is shown in Fig. S6 in Supplementary

342   Material.

343

344 3. Magnitude: We define the magnitude M as the logarithm of the maximum amplitude

345   of the seismic waves (as done for the observations) and assume that this amplitude

346   is proportional to the seismic moment $M_0 = \mu A d$ of the event, where μ, A, d is the

347   shear modulus, the slip area and the average slip value, respectively. Here, we

348   assume that the whole contact area slips during an event and that A is thus given by

349   Eq. (2). The frictional properties of glacial ice are known to be strongly dependent on

350   temperature, with a transition from slip-weakening (brittle) to slip-strengthening

351   (creep) characteristics for increasing temperatures (McCarthy et al., 2017). Thus, we

352   assume that seismic slip is limited by a maximum value E_d of the energy released per

353   unit area, where E_d is assumed to shift the temperature from the brittle into the creep

354   regime. If this constant is exceeded, ongoing slip is assumed to be aseismic, as a

355   result of reduced slip velocities due to velocity-strengthening. Because the released

356   energy is equal to force times slip, the seismic slip is thus assumed to be inversely

357   related to the normal stress, i.e., $E_d = \sigma_n d$. Consequently, the magnitude depends on

358   the Δ-value at the time of the event and is equal to:

359     $$M = \log_{10}\frac{\mu A E_d}{\sigma_n} = M_1 + \log_{10}\frac{A^2}{\Delta} \qquad (5)$$

360   where M_1 is a constant and A depends on Δ according to Eq. (2).

361

362 4. Hypocentre: The boundary conditions of the ice shelf relative to the source region are

363   asymmetric with a freely floating ice shelf on the ocean side, while the ice is fixed on

364   land. During high tides, the normal stress will be therefore smaller on the ocean side

365   of the local grounding feature and minimum at the edge of the contact area.

366   According to the Coulomb-Failure criterion (King et al., 1994), we assume that the

367   event will always nucleate at the ocean-side edge of the contact area, where CFS is

368   largest, which leads to the hypocentre location $x = \sqrt{A/\pi}$ measured relative to the

369   peak location (with x-axis directed towards the ocean and A given from Eq. (2)).

370

371   Model simulations are driven by the ocean tides, calculated for the given location by the

372   CATS2008a_opt model (Padman et al., 2002, 2008) during the analysed 80 days between

373   August and October 2013. The simulations depend only on three model parameters that

374   change the occurrence and magnitude patterns, namely (i) C, which determines the relative

375   strength of shear stress changes versus normal stress changes during tidal cycles; (ii) H,

376   which is the average height of the topographic peak of the shallow bedrock feature relative

377   to the bottom of the ice shelf; and (iii) the stress drop, S_Δ (see Table 1). The latter is fixed by

378   the condition that the total number of simulated events equals the observed ones, leading to

379    $S_\Delta = 0.03$, and H is set to the maximum tidal amplitude h which triggered an event in this

380   time period, namely $H = 0.8$ m. Thus, the only remaining free parameter is C, which effects

381   the phase distribution of the triggered events. The best model fit to the observed phase

382   distribution (see Fig. 4d) yields a value of $C = 0.7$. For smaller (larger) C-values, the model

383   predicts a later (earlier) onset of activity during the tidal cycles. All other patterns of the

384   simulated activity (Figs. 3a,c and 4a,c,d) are a direct outcome, without additional parameter

385   adjustments.

386

387   **4.2 Modelling results**

388   Most of the characteristics of the observed cryoseismicity can be well explained by the

389   proposed model (results shown by red symbols in Figs. 3 and 4). The model replicates well

390   the 14-day periodicity of the event rates (Fig. 3a). It also reproduces the general magnitude

391   trends, although it under-predicts the strength of the magnitude increase during cycles at

392   neap tides (Fig. 3b). The assumed unloading-loading mechanism also explains the quasi-

393   periodic recurrences (Fig. 4a), as well as the correlation of event frequency with the semi-

394   diurnal tide (Fig. 4b). In the latter case, however, the simulations show a narrower

395 distribution with an earlier maximum compared to observations. A possible 30 min delay of

396 the real tides relative to the calculated ones would better fit to our model results (blue line in

397 Fig. 4b). In the model, epicentres are assumed to occur at the ocean-side edge because of

398 smallest normal stress. As a result, epicentre locations are found to migrate landwards

399 during cycles with a constant speed (Fig. 4c). This is in agreement with the observed linear

400 trend of the change of the CC-time differences. Finally, the observed positive and negative

401 correlations between tidal heights and event magnitudes are reproduced (Fig. 4d), although

402 the model fails to reproduce the observed variability.

403

404 Based on the successful model fit of the activity between August and October 2013, we use

405 the model to understand the long-term trends of the observed seismicity. In the period

406 between 2012 and end 2015, the timing of the events within tidal cycles shows a systematic

407 trend that is strongly correlated to the trend of event magnitudes. During periods with larger

408 magnitudes, the events are also triggered at peak levels of the tide, whereas no events are

409 triggered at high tidal levels during phases with lower magnitudes. This is shown in the left

410 plot of Fig. 5b, where the maximum tidal value that triggered an event is compared to the

411 maximum tidal amplitude at this time and the event magnitudes. In terms of our model, this

412 correlation can be explained by a variation of the ice shelf thickness. The underlying physical

413 process is illustrated in Fig. 5c. A certain thickness of the ice shelf is necessary that it

414 grounds on an underlying bedrock shoal. When the shelf is thinner, no grounding and hence

415 no stick-slip seismic events occur. This might explain the absence of recorded activity before

416 2011 (Fig. 1c). The behaviour of a grounded shelf still depends on its thickness. A medium

417 thickness, much like the concept of ephemeral grounding (Schmeltz et al., 2001), will result

418 in seismic events at tidal amplitudes low enough that the coupling between ice and bedrock

419 is not lost, while the ice goes afloat, and no stick-slip events occur at high tidal levels. A

420 thicker shelf will have on average a larger contact area, which implies that slip along it will

421 produce events of larger magnitudes compared to a thinner shelf, while allowing for event

422 triggering to continue also for higher tidal amplitudes than previously. Since the installation

423 of station TROLL in February 2012, the largest event magnitudes have been observed

424 during our modelling interval in 2013, so we can assume that the ice shelf was thickest then.

425 To test the influence of different ice thickness W at other time periods, simulations were

426 repeated for different W values, keeping all other parameters constant. As a result, we find

427 an almost linear trend between ice thinning and the maximum tidal amplitude that triggers

428 events (right plot in Fig. 5b). This model result can be used for the calibration of the

429 observed variations during 2012 and 2015, which suggests variations of the ice shelf

430 thickness in the range of 0.5 m in this period.

431

432 **5. Discussion and conclusions**

433 A primary assumption when designing our model is that the ice shelf is locally grounded. In

434 the source region, the ice shelf is assumed to be generally afloat in shallow water (< 200 m),

435 but the available underwater topography is only based on a sparsely interpolated bathymetry

436 because of the inaccessible nature of the specific site (Nøst, 2004). The proximity to the

437 Kupol Moskovskij ice rise to the East and various ice rumples at the eastern side of

438 Trolltunga (Van Oostveen et al., 2017) suggests it is likely that the ice shelf is locally resting

439 on a shallow bathymetric feature. This is in agreement with the well-developed SH phases of

440 the recorded seismic waveforms (Fig. 2) that can only be generated with mechanical

441 coupling to the bedrock (e.g., Müller, 2007).

442

443 Although our mechanical model is based on simplifications of the complex nature of ice shelf

444 dynamics, it successfully explains most of the various distinctive features observed for the

445 recorded seismicity. These characteristics include strong determinism of the timing and

446 sizing of events. This contrasts with earthquakes, where the magnitudes and occurrence

447 times of subsequent earthquakes are usually uncorrelated and described by random

448 distributions, namely the Gutenberg-Richter distribution (Gutenberg and Richter, 1944) and

449   the Poisson model (e.g., Turcotte, 1992), respectively. This randomness is likely related to

450   earthquake interactions in complex crustal fault networks. The observed cryogenic seismicity

451   might act as a prototype for an isolated fault, which leads to a much higher predictability of

452   the system.

453

454   The time, magnitude, and migration patterns are well reproduced with only two model

455   parameters. The occurrence of stick-slip motion is predicted when Coulomb stress exceeds

456   a critical threshold value in the grounding area of the ice shelf. The assumed proportionality

457   of shear stressing rates to tidal amplitudes reproduces successfully the observed fortnightly

458   event rates. The daily event timing results from the competing effects of stress drops related

459   to the cryoseismic events and Coulomb stress loading by normal stress reduction during

460   increasing tides and continuous shear stress loading. The latter is essentially of constant

461   rate during the time scale of the triggered diurnal stick-slip sequences (Fig. S6 in

462   Supplementary Material). Event magnitudes depend on the rupture area; while the tide is

463   rising, the contact area gradually decreases, accounting for the decreasing magnitude trend

464   observed during semi-diurnal spring-tide cycles.

465

466   The only deviations between the model and observations concern the 30 min (~ 18°) delay

467   between the tide that would produce the best fit and the CATS2008a_opt tidal model, and

468   the failure of the model to reproduce the observed magnitude variability. The latter is likely

469   related to our simplified modelling of magnitudes that is not based on more appropriate

470   dynamic rupture modelling, which is outside the scope of the present study. The former may

471   too be related to neglected dynamic effects or healing properties, but might also be a

472   possible effect of actual bathymetry deviations from the geometry reflected in the tidal model

473   (e.g., Padman et al., 2018). Although GPS measurements at a distance of ~ 30 km (Kohler

474   and Langley, 2016), closer to the Kupol Moskovskij ice rise, show a good fit to the tidal

475   model (~ 10 – 15 min phase deviations), discrepancies from actual bathymetry might be

476   more pronounced at the source region. Robel et al. (2017) consider phase lags between

477   measured horizontal ice-displacement variations and tidal heights as indicators of stress

478   variations, in settings where ice shelf/sheet grounding occurs. Small lags suggest that strain

479   and the modulation of ice flow are dominated by back-stress variations rather than

480   hydrostatic stresses. In our source region, known and uncharted local grounding points (i.e.,

481   ice rises and rumples) introduce resistance to ice flow (e.g., Schmeltz et al., 2001; Favier et

482   al., 2016). Our model is very similar in concept to that of Robel et al. (2017), exploring the

483   same processes from a different scope.

484

485   Based on the interpretation above, we propose that the lack of similar cryoseismic activity in

486   our study region prior to late 2011 is connected to a reduced thickness of the ice shelf that

487   keeps it afloat. A gradual increase of about 0.5 m takes place from late 2011 through 2013,

488   resulting in the intense seismicity levels between August and October 2013. This phase is

489   followed by some minor thinning of about 0.3 m, to account for the smaller event magnitudes

490   observed in 2015. Recent studies of Antarctic ice discharge (Gardner et al., 2018; Shen et

491   al., 2018) find no significant ice thickness variations for DML over the past 7 years, while

492   studies going back to 2003 find slight variations (both positive and negative) at various

493   locations (Horwath et al., 2012). However, relevant uncertainties in those studies are far

494   larger than the thickness variations discussed herein. Our observations concern a very local

495   scale and results from dedicated studies are required for a proper comparison. The origins

496   of the inferred variation in ice thickness (e.g., advection, changes in accumulation or melting)

497   are outside the scope of this paper. It is noteworthy that the seasonal fluctuations (i.e., more

498   seismic activity winter to spring, less summer to autumn) coincide fairly well with the

499   seasonal melt rates beneath the FIS (Abrahamsen, 2012) that control ice shelf thickness,

500   maxima near the ocean front occurring during the austral summer.

501

502　Our model explains both the short-term oscillatory seismicity patterns and the long-term

503　trend of the observations, with the fluctuation of seismic activity levels, including the lack

504　thereof. It thus provides independent evidence of localised variations in ice-shelf thickness

505　and a means to identify ephemeral grounding points.

506

535 **Author contributions**

536 M.P. compiled the dataset, carried out seismic waveform analysis and collected non-

537 seismological data. M.P. and J.S. performed CC event detection and location. A.K.

538 performed HMM event detection. S.H. and T.D. developed the model. S.H. implemented the

539 model and ran the simulations. All authors contributed to the interpretation of the results and

540 to writing the manuscript.

541

542 **References**

543 Abrahamsen, E.P. (2012). Oceanographic conditions beneath Fimbul Ice Shelf, Antarctica.

544   Doctoral Thesis, University of Southampton, School of Ocean and Earth Science.

545 Barruol, G., Cordier, E., Bascou, J., Fontaine, F.R., Legrésy, B. and Lescarmontier, L.

546   (2013). Tide-induced microseismicity in the Mertz glacier grounding area, East Antarctica.

547   Geophys. Res. Lett., 40, 5412-5416, doi:10.1002/2013GL057814.

548 Bayer, B., Geissler, W.H., Eckstaller, A. and Jokat, W. (2009). Seismic imaging of the crust

549   beneath Dronning Maud Land, East Antarctica. Geophys. J. Int., 178, 860-876,

550   doi:10.1111/j.1365-246X.2009.04196.x.

551 Bindschadler, R.A., King, M.A., Alley, R.B., Anandakrishnan, S. and Padman, L. (2003).

552   Tidally controlled stick-slip discharge of a West Antarctic ice stream. Science, 301, 1087-

553   1089, doi: 10.1126/science.1087231.

554 Brotchie, J.F. and Silvester, R. (1969). On crustal flexure. J. Geophys. Res., 74, 5240-5252,

555   doi:10.1029/JB074i022p05240.

556 Brunt, K.M., Fricker, H.A. and Padman, L. (2011). Analysis of ice plains of the Filchner-

557   Ronne Ice Shelf, Antarctica, using ICESat laser altimetry. J. Glaciology, 57, 965-975,

558   doi:10.3189/002214311798043753.

559 Favier, L., Patty, F., Berger, S. and Drews, R. (2016). Dynamic influence of pinning points on

560   marine ice-sheet stability: a numerical study in Dronning Maud Land, East Antarctica. The

561   Cryosphere, 10, 2623-2635, doi:10.5194/tc-10-2623-2016.

562 Gardner, A.S., Moholdt, G., Scambos, T., Fahnstock, M., Ligtenberg, S., van den Broecke,

563   M. and Nilsson, J. (2018). Increased West Antarctic and unchanged East Antarctic ice

564   discharge over the last 7 years. The Cryosphere, 12, 521-547, doi:10.5194/tc-12-521-

565   2018.

566 Gibbons, S.J. and Ringdal, F. (2006). The detection of low magnitude seismic events using

567   array-based waveform correlation. Geophys. J. Int., 165, 149-166, doi: 10.1111/j.1365-

568   246X.2006.02865.x.

569 Gutenberg, B. and Richter, C.F. (1944). Frequency of earthquakes in California. Bull.

570   Seismol. Soc. Am., 34, 185-188.

571 Hammer, C., Ohrnberger, M. and Fäh, D. (2013). Classifying seismic waveforms from

572   scratch: a case study in the alpine environment. Geophys. J. Int., 192, 425-439,

573   doi:10.1093/gji/ggs036.

574 Hammer, C., Ohrnberger, M. and Schlindwein, V. (2015). Pattern of cryospheric seismic

575   events observed at Ekström Ice Shelf, Antarctica. Geophys. Res. Lett., 42, 39363943,

576   doi:10.1002/2015GL064029.

577 Havskov, J., Bormann, P. and Schweitzer, J. (2012) Seismic source location. IS11.1 in: New

578   Manual of Seismological Observatory Practice (NMSOP-2), Bormann, P. Ed., IASPEI,

579   GFZ German Research Centre for Geosciences, Potsdam, 36 pp.,

580   doi:10.2312/GFZ.NMSOP-2_IS_11.1.

581 Horwath M., Legrésy, B., Rémy, F., Blarel, F. and Lemoine, J.-M. (2012). Consistent

582   patterns of Antarctic ice sheet interannual variations from ENVISAT radar altimetry and

583   GRACE satellite gravimetry. Geophys. J. Int., 189, 863-876, doi:10.1111/j.1365-

584   246X.2012.05401.x.

585   Hulbe, C.L., Klinger, M., Masterson, M., Catania, G., Cruikshank, K. and Bugni, A. (2016).

586   Tidal bending and strand cracks at the Kamb Ice Stream grounding line, West Antarctica.

587   J. Glaciology, 62, 816-824, doi:10.1017/jog.2016.74.

588   Humbert, A. and Steinhage, D. (2011). The evolution of the western rift area of the Fimbul

589   Ice Shelf, Antarctica. The Cryosphere, 5, 931-944, doi:10.5194/tc-5-931-2011.

590   Jha, S., Harry, D. L. and Schutt, D. L. (2017). Toolbox for Analysis of Flexural Isostasy

591   (TAFI) – A MATLAB toolbox for modeling flexural deformation of the lithosphere.

592   Geosphere, 13, 1555-1565, doi:10.1130/GES01421.1.

593   King, G. C. P., Stein, R. S. and Jian, L. (1994). Static stress changes and the triggering of

594   earthquakes. Bull. Seismol. Soc. Am., 84, 935-953.

595   [dataset] Kohler, J. and Langley, K. (2016). GPS Profiles Fimbulisen Ice Shelf 2009-2012.

596   Norwegian Polar Institute, doi:10.21334/npolar.2016.664d3c4c.

597   Lombardi, D., Benoit, L., Camelbeeck, T., Martin, O., Meynard, C. and Thom, C. (2016).

598   Bimodal pattern of seismicity detected at the ocean margin of an Antarctic ice shelf.

599   Geophys. J. Int., 206, 1375-1381, doi:10.1093/gji/ggw214.

600   Matsuoka, K., Hindmarsh, R.C.A., Moholdt, G., Bentley, M.J., Pritchard, H.D., Brown, J.,

601   Conway, H., Drews, R., Durand, G., Goldberg, D., Hatermann, T., Kingslake, J., Lenaerts,

602   J.T.M., Martín, C., Mulvaney, R., Nicholls, K.W., Pattyn, F., Ross, N., Scambos, T. and

603   Whitehouse, P.L. (2015). Antarctic ice rises and rumples: Their properties and

604   significance for ice-sheet dynamics and evolution. Earth-Sci. Rev., 150, 724-745,

605   doi:10.1016/j.earscirev.2015.09.004.

606   Matsuoka, K., Skoglund, A. and Roth, G. (2018). Quantarctica [3]. Norwegian Polar Institute,

607   Tromsø, Norway, doi:10.21334/npolar.2018.8516e961.

608 McCarthy, C., Savage, H. and Nettles, M. (2017). Temperature dependence of ice-on-rock

609   friction at realistic glacier conditions. Phil. Trans. R. Soc. A, 375, 20150348,

610   doi:10.1098/rsta.2015.0348.

611 Mouginot, J., Scheuchl, B. and Rignot, E. (2012). Mapping of ice motion in Antarctica using

612   Synthetic-Aperture Radar data. Remote Sensing, 4, 2743-2767, doi:10.3390/rs4092753.

613 Müller, G. (2007). Theory of Elastic Waves. Weber, M., Rümpker, G. and Gajewski, D. Eds,

614   Sci. Techn. Rep. STR 07/03, 229 pp., GeoForschungsZentrum Potsdam, Potsdam,

615   doi:10.2312/GFZ.b103-07037.

616 Murray, T., Smith, A.M., King, M.A. and Weedon, G.P. (2007). Ice flow modulated by tides at

617   up to annual periods at Rutford Ice Stream, Antarctica. Geophys. Res. Lett., 34, L18503,

618   doi:10.1029/2007GL031207.

619 Nøst, O.A. (2004). Measurements of ice thickness and seabed topography under the Fimbul

620   Ice Shelf, Dronning Maud Land, Antarctica. J. Geophys. Res., 109, C10010,

621   doi:10.1029/2004JC002277.

622 Padman, L., Fricker, H.A., Coleman, R., Howard, S. and Erofeeva, L. (2002). A new tide

623   model for the Antarctic ice shelves and seas. Ann. Glaciology, 34, 247-254, doi:

624   10.3189/172756402781817752.

625 Padman, L., Erofeeva, S.Y. and Fricker, H.A. (2008). Improving Antarctic tide models by

626   assimilation of ICESat laser altimetry over ice shelves. Geophys. Res. Lett., 35, L22504,

627   doi:10.1029/2008GL035592.

628 Padman, L., Siegfried, M.R. and Fricker, H.A. (2018). Ocean tide influences on the Antarctic

629   and Greenland ice sheets. Rev. Geophysics, 56, 142-184, doi:10.1002/2016RG000546.

630 Podolskiy, E.A., Sugiyama, S., Funk, M., Walter, F., Genco, R., Tsutaki, S., Minowa, M. and

631   Ripepe, M. (2016). Tide-modulated ice flow variations drive seismicity near the calving

632   front of Bowdoin Glacier, Greenland. Geophys. Res. Lett., 43, 20362044, doi:

633   10.1002/2016GL067743.

634   Rignot, E., Mouginot, J. and Scheuchl, B. (2011). Ice flow of the Antarctic ice sheet. Science,

635   333, 1427-1430, doi:10.1126/science.1208336.

636   [dataset] Rignot, E., Mouginot, J. and Scheuchl, B. (2017). MEaSURES InSAR-based

637   Antarctica ice velocity map, Version 2. NASA National Snow and Ice Data Center

638   Distributed Active Archive Center, Boulder, Colorado USA, doi:10.5067/D7GK8F5J8M8R.

639   Robel, A.A., Tsai, V.C., Minchew, B. and Simons, M. (2017). Tidal modulation of ice shelf

640   buttressing stresses. Ann. Glaciology, 58, 12-20, doi:10.1017/aog.2017.22.

641   Sayag, R. and Worster, M.G. (2013). Elastic dynamics and tidal migration of grounding lines

642   modify subglacial lubrication and melting. Geophys. Res. Lett., 40, 5877-5881,

643   doi:10.1002/2013GL057942.

644   Schmeltz, M., Rignot, E. and MacAyeal, D.R. (2001). Ephemeral grounding as a signal of

645   ice-shelf change. J. Glaciology, 47, 71-77, doi:10.3189/172756501781832502.

646   Schweitzer, J. (2001). HYPOSAT – an enhanced routine to locate seismic events. Pure

647   Appl. Geophysics, 158, 277-289, doi:10.1007/PL00001160.

648   Schweitzer, J. (2013). Automatic parameter extraction for three-component observations.

649   NORSAR Sci. Rep., 2-2012, 36-49.

650   Schweitzer, J. (2018). User Manual for HYPOSAT 6 and HYPOMOD 2. In: New Manual of

651   Seismological Observatory Practice (NMSOP-3), Bormann, P. Ed., IASPEI, GFZ German

652   Research Centre for Geosciences, Potsdam, 38 pp., doi:10.2312/GFZ.NMSOP-

653   3_PD_11.1.

654   Schweitzer, J., Fyen, J., Mykkeltveit, S., Gibbons, S.J., Pirli, M., Kühn, D. and Kværna, T.

655   (2012). Seismic Arrays. Chapter 9 in: New Manual of Seismological Observatory Practice

656   (NMSOP-2), Bormann, P. Ed., IASPEI, GFZ German Research Centre for Geosciences,

657   Potsdam, 80 pp., doi:10.2312/GFZ.NMSOP-2_CH9.

658   Schweitzer, J., Pirli, M., Roth, M. and Kværna, T. (2014). TROLL: A new, very broadband

659   seismic station in Antarctica. Seismol. Res. Lett., 85, 852-862, doi:10.1785/0220130223.

660   Shen, Q., Wang, H., Shum, C.K., Jiang, L., Hsu, H.T. and Dong, J. (2018). Recent high-

661   resolution Antarctic ice velocity maps reveal increased mass loss in Wilkes Land, East

662   Antarctica. Sci. Rep., 8, 4477, doi:10.1038/s41598-018-22765-0.

663   Torsvik, A. (2015). Seismic imaging of the crust beneath TROLL seismic station in Queen

664   Maud Land, Antarctica. Master Thesis, University of Oslo.

665   Tsai, V.C. and Gudmundsson, G.H. (2015). An improved model for tidally modulated

666   grounding-line migration. J. Glaciology, 61, 216-222, doi:10.3189/2015JoG14J152.

667   Turcotte, D.L. (1992). Fractals and chaos in geology and geophysics. Cambridge University

668   Press, New York, xii+416 pp.

669   Van Oostveen, J., Moholdt, G., Kääb, A. and Matsuoka, K. (2017). Gradual slowdown and

670   thickening of Fimbulisen ice shelf, East Antarctica, over the past decade. Geophys. Res.

671   Abstracts, 19, EGU2017-15507.

672   Vaughan, D.G. (1995). Tidal flexure at ice shelf margins. J. Geophys. Res., 100, B4, 6213-

673   6224, doi:10.1029/94JB02467.

674   Wessel, P., Smith, W.H.F., Scharroo, R., Luis, J.F. and Wobbe, F. (2013). Generic Mapping

675   Tools: Improved version released. EOS Trans. AGU, 94, 409-410,

676   doi:10.1002/2013EO450001.

677   Winberry, J.P., Anandakrishnan, S., Alley, R.B., Wiens, D.A. and Pratt, M.J. (2014). Tidal

678   pacing, skipped slips and the slowdown of Whillans Ice Stream, Antarctica. J. Glaciology,

679   60, 795-807, doi:10.3189/2014JoG14J038.

680   Zoet, L. K., Anandakrishnan, S., Alley, R. B., Nyblade, A. A. and Wiens, D. A. (2012). Motion

681   of an Antarctic glacier by repeated tidally modulated earthquakes. Nature Geosc., 5, 623-

682   626, doi:10.1038/ngeo1555.

683

684

685

686

Table 1

688   Model parameters with their meaning and values.

Parameter	Description	Value
z_0	Average elevation of the sea level	n.s.[a]
$h(t)$	Tidal height relative to z_0	CATS2008a_opt
W, W_{2013}	Thickness of the ice shelf (W_{2013} value in 2013)	n.s.
$z_1(t) = z_0 + h(t) - 0.9\ W, <z_1>_{2013}$	Elevation of bottom of a freely floating ice shelf ($<z_1>_{2013}$: average in 2013)	n.s.
z_2	Peak elevation of the bedrock protrusion	n.s.
$\Delta(t) = z_2 - z_1(t)$	Relative elevation of the bedrock peak to the ice shelf bottom	
$H = <\Delta>_{2013} = z_2 - <z_1>_{2013}$	Height of the pinning point above $<z_1>_{2013}$	0.8 m
$A(t)$	Area of the contact zone between ice and bedrock	Eq. (2)
R_{max}	Radius of the maximum contact area	n.s.
$\dot{\tau}_0$	Average shear stressing rate	n.s.
$E_h(t), <E_h>$	Amplitude of the tidal variations ($<E_h>$: average value)	calculated from $h(t)$, see Fig. 3a
$\tau(t) = \tau(t_0) + \dot{\tau}_0 \int_{t_0}^{t} E_h(\tilde{t})/\langle E_h \rangle d\tilde{t}$	Shear stress (after last event at time t_0)	
$\sigma_n(t) = c_f\ \Delta(t)\ /\ A(t)$	Normal stress (c_f: proportionality factor)	
f	Friction coefficient	n.s.
$CFS(t) = \tau(t) - f\ \sigma_n(t)$	Coulomb Failure stress	Eq. (3)
$\widetilde{CFS} = f\ c_f\ H\ /\ (\pi\ R^2_{max})$	Normalization factor	n.s.
$S(t) = CFS(t)\ /\ \widetilde{CFS}$	Normalized CFS	Eq. (4)
$C = \dot{\tau}_0/\widetilde{CFS}$	Normalized (average) shear stressing rate	0.7
$S_\Delta = \Delta_\tau/\widetilde{CFS}$	Normalized value of the stress drop associated with slip	0.03
$M = M_1 + \log_{10}(A^2/\Delta)$	Event magnitude (constant M_1 is set to 0)	Eq. (5)

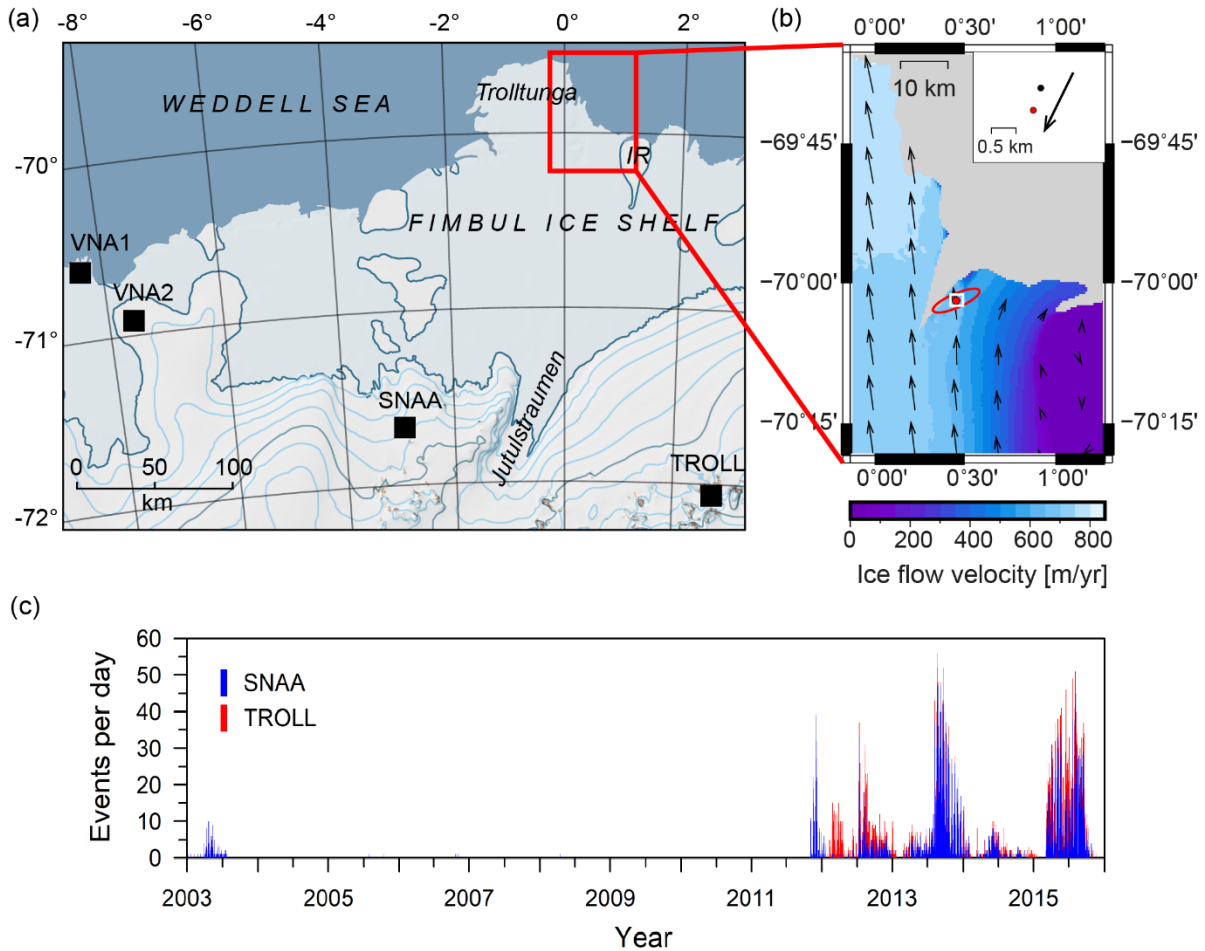689   [a] n.s. refers to values which do not need to be specified.

690

691

692

693

694

695

696

Fig. 1. Geographic and temporal aspects of observed cryoseismicity. (a) Map of western

DML. Grounded ice is in white, floating ice shelf in light blue, ocean in blue and bedrock

outcrops in brown. Thin contour lines are topography in 200 m increments. The locations of

permanent seismic stations in the region are noted with black squares. IR marks the Kupol

Moskovskij ice rise. The red rectangle encloses the source region of the cryoseismic activity

shown in panel (b). (b) The cryoseismicity source region. The red circle notes the absolute

location result for the source of the large cryoseismic event that occurred on 9 September

2013. The overall uncertainty of this estimate is expressed by the 95% confidence-level error

ellipse, shown in red. The colour scale describes ice flow velocity in m/yr and the vectors

show direction of flow (Mouginot et al., 2012; Rignot et al., 2011, 2017), scaled to a

maximum of 850 m/yr. The white rectangle encloses the area in the inlet, that shows the

absolute location epicentre in red and the relative location estimate in black, the arrow noting

the direction of epicentre migration. (c) Number of cryoseismic events per day from 2003 to

710   end 2015 (no detections between 1997 and 2003), based on the results of the CC-detector

711   at SNAA (blue) and TROLL (red).

712

713
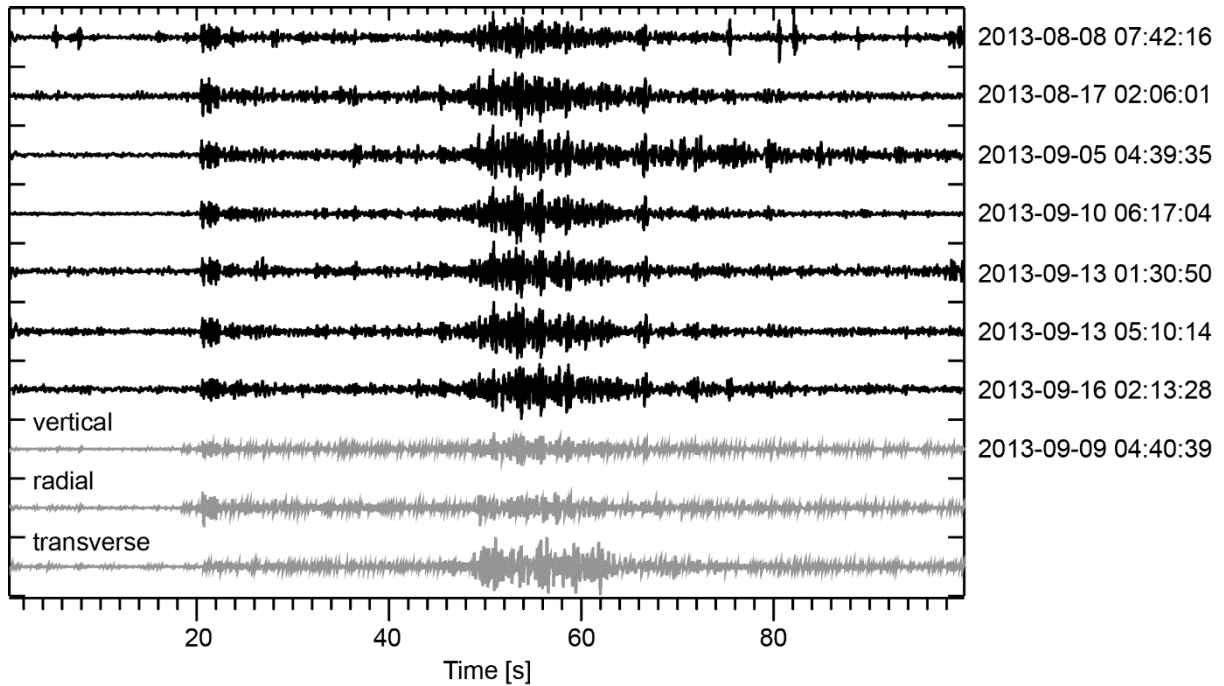
714

715   Fig. 2. Examples of highly similar events (multiplets), as recorded at TROLL. Waveforms are

716   bandpass filtered between 2 and 6 Hz. The vertical component is shown for waveforms in

717   black, normalized to maximum amplitude. Waveforms in grey show the vertical and rotated

718   horizontal components of the located event on 9 September 2013, scaled to the maximum

719   amplitude. Note the well-developed S-wave onset on the transverse component (SH).

720

721
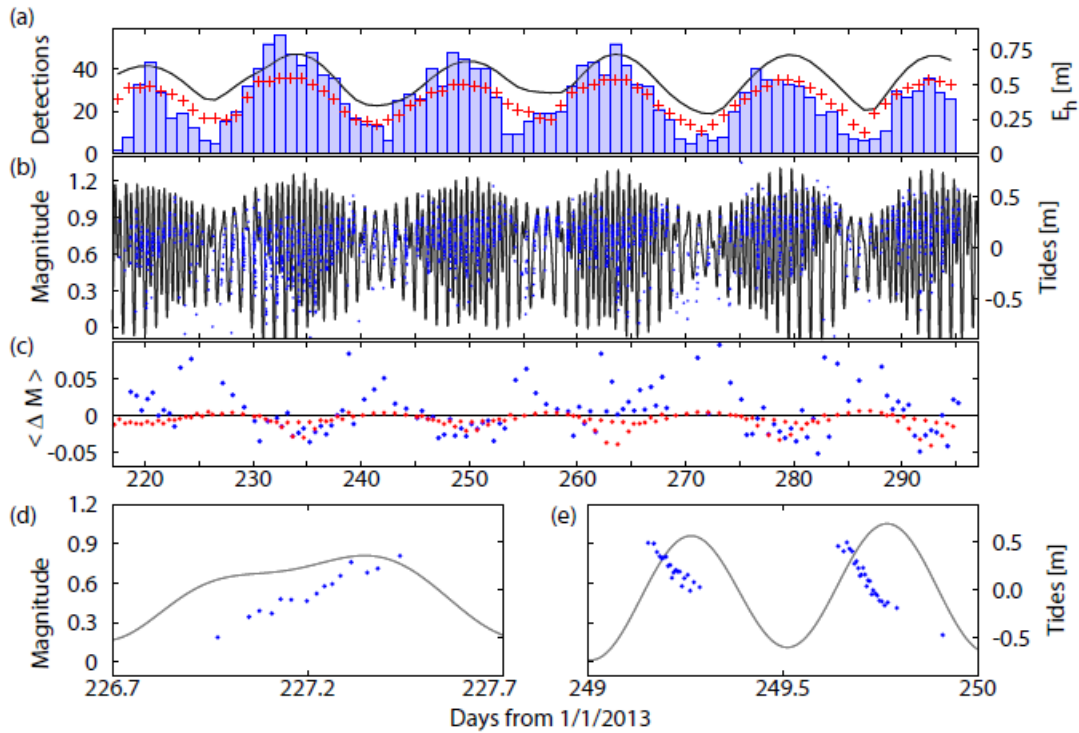
722

723   Fig. 3. Time series of observations (blue) in comparison to simulations (red). (a) Histogram

724   of daily numbers of events at station TROLL in comparison to the envelope amplitude E_h of

725   the tidal signal (grey line), as predicted by the CATS2008a_opt tidal model (Padman et al.,

726   2002, 2008) for the cryoseismicity source region, between 5 August and 24 October 2013.

727   (b) Event magnitudes versus occurrence times, where the ocean tides are shown by grey

728   line. (c) The average magnitude difference, $\langle \Delta M \rangle$, between successive events within

729   temporal clusters as function of time, indicating negative trends during spring tides and

730   increasing magnitudes during neap tides. Each point refers to the result of one cluster, which

731   is defined by a sequence of minimum 5 events with inter-event times less than 6 hours.

732   (d),(e) Two examples of the magnitude trend within individual clusters, each cluster

733   represented by one point in (c).

734

735
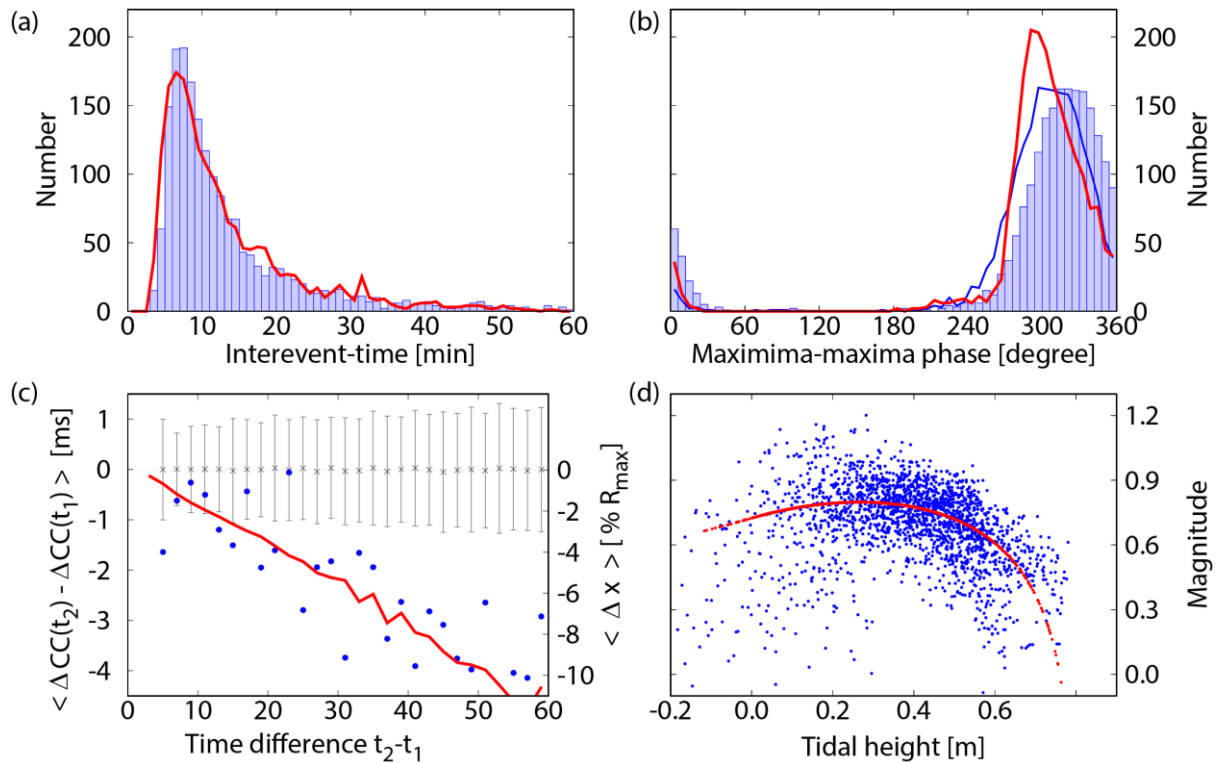
Fig. 4. Observed (blue) and modelled (red) characteristics. (a) Distribution of inter-event times between successive events. (b) Histogram of the relative occurrence times of events between two successive maxima of the tides (phase between 0° and 360°). The blue line indicates the result if a delay of 30 min is assumed for the true tides with respect to the tides calculated by the CATS2008a_opt model (Padman et al., 2002, 2008). (c) The average change of the delay time, ΔCC, between the detections at stations TROLL and SNAA, as function of the time difference between events. The error bars refer to the same result plus/minus one standard deviation for the randomly reshuffled ΔCC-times. The observed trend indicates migration which is in agreement with the linear trend in the simulations, where Δx is the difference of the epicentre position and R_{max} the maximum radius of the contact area. (d) Magnitude of the events as function of the tidal height.
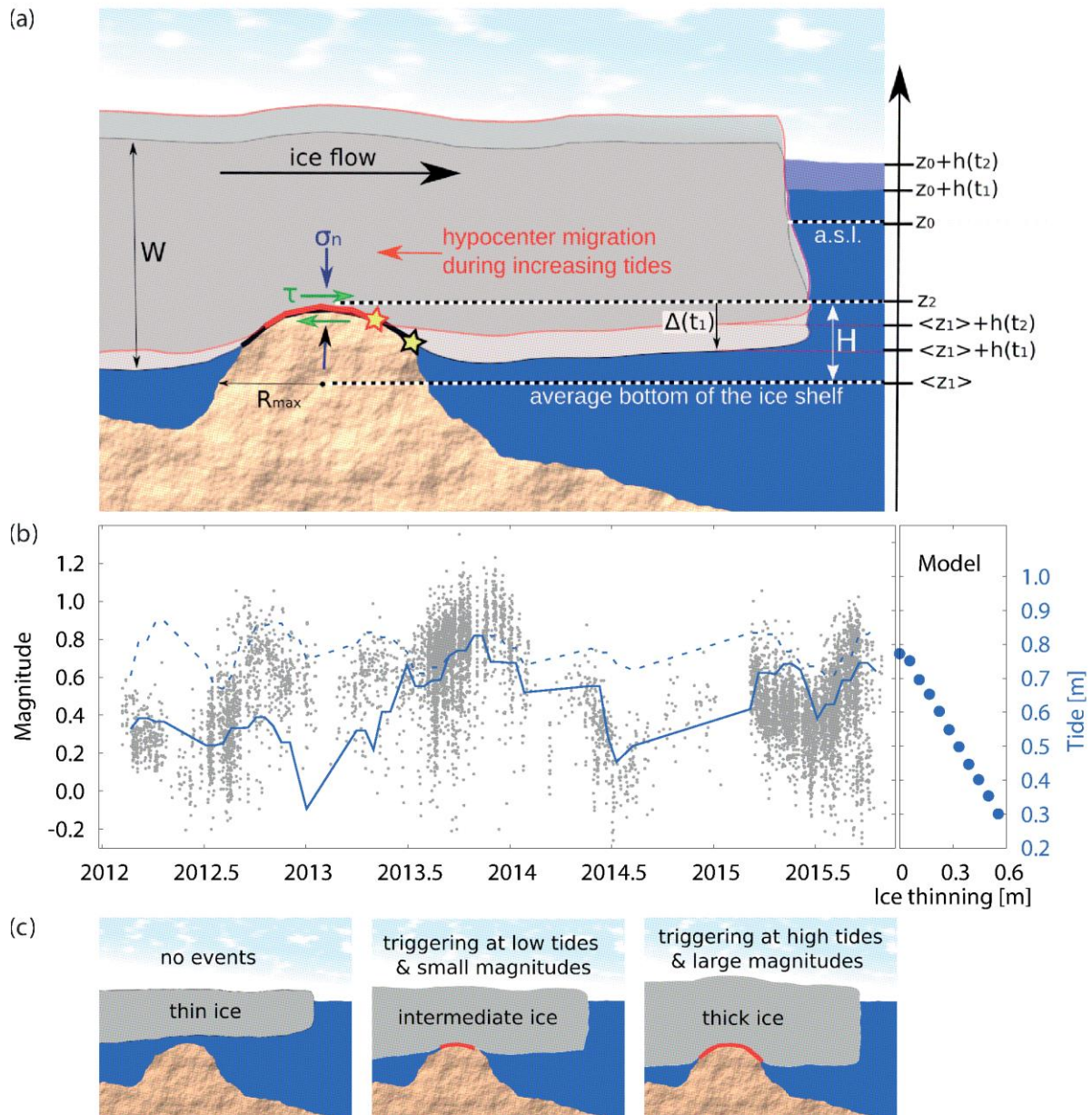
Fig. 5. Model setup and ice thickening as explanation for the long-term trend. (a) Illustration of the assumed stick-slip motion at a bedrock protrusion (pinning point), where the ice shelf becomes locally grounded. The pinning point is depicted in a generic form, with exaggerated topography to facilitate recognition of model parameters. 90% of the shelf is below the average sea level (a.s.l.). Tidal variations (h) change the normal and shear stress, as well as the contact area between bedrock and shelf ice. H defines the height of the shallow bathymetric feature relative to the average position of the bottom of the ice shelf in the period between August and October 2013. Here, increasing tides are assumed ($dh/dt > 0$),

759　　so the contact area decreases due to the decreasing difference $Δ = H – h$ (see section 2.5),

760　　leading to a migration of the hypocentres (stars) and reduced rupture areas (black/red lines).

761　　(b) Event magnitudes versus occurrence times recorded between 2012 and end 2015 (grey

762　　dots). The magnitude trend is found to correlate with the timing of the events within the tidal

763　　cycles. The solid, blue curve shows the maximum tidal values that triggered events, while

764　　the dashed, blue line indicates the maximum tidal amplitude at this time (scale on right:

765　　calculated for time bins of 30 days with a minimum of 50 events). The plot on the right shows

766　　the maximum triggering tide as function of ice-shelf thickness decrease in the model

767　　simulations (without changing any other parameters). (c) Illustration summarising the

768　　general effects of varying ice thickness in different time periods.